(Received 4 March 2026, Accepted 15 April 2026, Scheduled 2 May 2026)

Dual-Band Crescent-Shaped Microstrip Antenna Using Peripheral Slits and Mutual Coupling Enhancement for Wi-Fi and Agriculture Applications

Lina Andriani[1], Nurhayati Nurhayati[1,*], Akbar Izulhaq[1], Usman R. Iman[2], Wa'il A. G. Al-Tumah[3], Atul Varshney[4,5], Mahmud Ja'afar[6], Sayyidul A. Alamsyah[1], and Fannush S. Akbar[7]

[1]*Department of Electrical Engineering, Universitas Negeri Surabaya, Surabaya 60231, Indonesia*
[2]*Department of Electronic Engineering, Hanyang University, Seoul 04763, South Korea*
[3]*Department of Physics, College of Science, University of Basrah, Iraq*
[4]*ECE Department, Gurukul Kangri (Deemed to be University), Haridwar, Uttarakhand 249404, India*
[5]*Graphic Era (Deemed to be University), Dehradun, Uttarakhand 248002, India*
[6]*Department of Electronics and Telecommunications Engineering, Ahmadu Bello University, Zaria, Nigeria*
[7]*The University Center of Excellence for Intelligent Sensing-IoT, Telkom University, Surabaya, Indonesia*

ABSTRACT: This study presents the design and analysis of a compact dual-band crescent-shaped microstrip antenna that utilizes edge slots and mutual coupling enhancement techniques for Wi-Fi 2.4/5.8 GHz and agricultural communication technologies. A mutual coupling enhancement structure was added to stabilize the impedance and strengthen the dual-band performance. The antenna was implemented on an FR-4 substrate with a thickness of 1.6 mm and a dielectric constant of 4.3. We compared four antenna elements, i.e., circular patch with circular hole (CwCh), circular crescent patch (CC), circular crescent peripheral slit patch (CCPS), and circular crescent peripheral slit with ring patch (CCPSR). The simulation results show that the CwCh antenna element produced the largest number of resonance frequencies, and the CCPSR antenna element produces the best minimum S_{11} of -40.49 dB at 3.56 GHz. We compared six types of MIMO 2×1 CCPSR antennas. CCPSR-5 produced minimum S_{11} of -30.36 dB (at 2.45 GHz) and -28.08 dB (at 5.8 dB). By adding a rectangular slot between the two antenna elements on the ground and adding three rectangular split ring resonators between the two antenna elements, the CCPSR improved the mutual coupling performance by 15.32 dB. The combination of peripheral slots and mutual coupling enhancement effectively improved the resonance frequency, resulting in a multiband frequency and mutual coupling performance. Both the modeling and measurement data indicated that the antenna performed similarly. The antenna's performance was assessed for soil pH and moisture data transmission, ensuring reliable device enrollment within the smart agricultural infrastructure. These results demonstrate that the proposed crescent-shaped antenna provides an efficient and versatile solution for compact Wi-Fi infrastructure, effectively fostering innovation in next-generation communication systems.

1. INTRODUCTION

The development of wireless communication technology continues to increase in line with the growing demand for high data capacity, spectrum efficiency, and compact devices. Wi-Fi technology has generated significant economic growth [1]. According to the Wi-Fi Alliance, this technology plays a very important role in human life, especially in increasing the growth of the Internet of Things (IoT), smart home systems, and portable devices, which increases the need for antennas that are compact, lightweight, inexpensive, and capable of operating in various frequency bands [2]. According to the IEEE 802.11 be or Wi-Fi 7 standard, the parameter criteria are as follows: bandwidth of 40, 80, 160, and 320 MHz; use of the multiple-input multiple-output (MIMO) transmission system; impedance of 50 Ω; 4K-QAM, gain of 4–8 dB; and resonant frequencies of 2.4 GHz (2.400–2.4835 GHz), 5 GHz (5.725–5.859 GHz), and 6 GHz (5.925–6.425 GHz, 6.425–6.525 GHz, 6.525–6.875 GHz, and 6.875–7.125 GHz) [3–5].

Microstrip antennas are commonly used in Wi-Fi devices owing to their simple fabrication, low cost, and small size [6]. However, microstrip antennas have certain disadvantages, such as narrow bandwidth, limited gain, and low power. Rectangular patches or conventional layouts often struggle to produce natural dual resonance, requiring miniaturization techniques such as the introduction of slots, gaps, or geometric disturbances to support multiband characteristics [7]. However, achieving a stable dual-band operation remains challenging.

Various approaches have been developed to improve dual-band performance, including the use of C-slots, U-slots, metamaterial-based configurations, and multi-resonator structures. U-shaped slot designs can produce two independent current paths that support dual resonance [8], whereas a combination of slots on patches and ground planes has been successfully applied to FR-4 Wi-Fi/WiMAX antennas [9]. Modifications to the geometric slots and radiator-ground have also been reported to expand the impedance bandwidth and increase gain without requiring additional layers [10]. The

* Corresponding author: Nurhayati Nurhayati (nurhayati@unesa.ac.id).

concepts of metasurfaces and artificial magnetic conductors (AMCs) further provide miniaturization and gain enhancement [11]. Additionally, the installation of complementary split-ring resonators (CSRRs) can increase bandwidth, gain, and controllable band rejection characteristics; however, resonator-based solutions generally increase structural complexity and fabrication limitations [12–14]. As an alternative, bandwidth enhancement can be achieved through simple geometric modifications to the radiator and ground plane, wherein slot loading and curve formation have been shown to significantly expand impedance bandwidth and increase gain without requiring additional resonators or multilayer structures [15].

Similarly, resonator-based designs that use separate ring resonators (SRRs) or complementary SRRs (CSRRs), including those implemented on 3D printed substrates, can provide dual-band performance; however, they often rely on unconventional fabrication processes that are less suitable for low-cost applications. Dual-band performance can also be achieved using parasitic elements, defective ground structures (DGSs), and U-slot geometries. Although these techniques can expand bandwidth and increase the gain, they often result in large antenna dimensions or unstable impedance characteristics. In addition to planar geometry-based slot approaches, modern research has begun integrate more complex slot-loading and leaky-wave mechanisms to further enhance the bandwidth, gain, and scanning capabilities [16].

In the context of multiple-input-multiple-output (MIMO) systems, metamaterial and metasurface unit cells have proven effective in reducing electromagnetic coupling and improving radiation efficiency [17]. However, many metamaterial structures for millimeter-wave and sub-6 GHz applications require multi-layer fabrication with tight dimensional tolerances, making them less attractive for compact, low-cost Wi-Fi terminals. In contrast, simpler resonators, such as meandered line structures, parasitic strips, or defective ground patterns, have also been reported to reduce mutual coupling without requiring overly complex geometries [18]. Miniature U-slot and coplanar waveguide (CPW)-fed planar antennas have been experimentally proven to produce stable dual resonance and broadband characteristics in several wireless bands [19]. However, these features come at the expense of increased geometric complexity and challenging fabrication, particulary when extended to multiport MIMO configurations.

Given these challenges, a simpler geometric approach is needed that provides stable dual-band performance, adequate bandwidth, good radiation efficiency, and controlled mutual coupling. One potential solution is to use a crescent-shaped antenna geometry. This geometry provides two current paths with different electrical lengths, thereby enabling dual resonance without requiring additional resonators, such as SRRs/CSRRs or complex multilayer metasurfaces. Studies on circular microstrip structures and cut discs have shown that an asymmetric current path distribution can produce dual resonance with increased stability and controlled coupling and performance [20].

To further improve performance, the crescent-shaped design in this study was optimized using peripheral slots to extend the current path, increase bandwidth, and support miniaturization while maintaining structural simplicity, in comparison to conventional multislot designs. Additionally, a simple resonant structure was placed at the center of the geometry. This structure functions as a mutual coupling enhancement (or suppression) element that operates similarly to a planar metamaterial resonator, producing artificial resonance paths while stabilizing the back-loss characteristics on both Wi-Fi bands. This approach enables impedance performance improvement without requiring complex layered metasurface arrays or dense SRR/CSRR inclusions

This research's originality and primary contributions are summarized as follows:

1. Four antenna elements, namely circular patch with a circular hole (CwCh), circular crescent Patch (CC), circular crescent peripheral slit patch (CCPS), and Circular Crescent Peripheral Slit with Ring Patch (CCPSR), were varied to realize multiple frequency bands with target dual-band frequencies of 2.4 and 5.8 GHz.

2. Several methods for reducing mutual coupling on a 2×1 antenna element using a slot in the center of the ground plane between the two antennas and a rectangular split-ring resonator between the two elements on the side of the patch antenna to improve the antenna's isolation performance are presented in this study.

3. Fabricating and integrating an antenna for IoT and agriculture application.

Thus, this study aims to present an efficient, simple, and stable dual-band microstrip antenna design by leveraging the advantages of crescent geometry and enhancing performance through peripheral slots and antenna isolation enhancement structures.

2. ANTENNA DESIGN

The proposed antenna uses a printed planar patch configuration with a crescent-shaped patch and edge slots to achieve dual-band operation in the 2.4 GHz and 5.8 GHz Wi-Fi bands. This antenna is implemented on a low-cost FR-4 substrate with a relative permittivity of 4.3 and a thickness of 1.6 mm. A microstrip feed line with a characteristic impedance of 50 Ω is used to drive the radiator, where W_f and L_f denote the width and length of the feed line respectively.

The final geometric parameters of the proposed antenna were obtained through an extensive parametric optimization process to ensure stable impedance matching and reliable dual-band operation. The optimized antenna occupied a total substrate area of $52 \times 35 \times 1.6\,\text{mm}^3$, providing a compact footprint while maintaining sufficient ground plane support. The crescent-shaped radiator is characterized by its outer and inner effective radii, which govern the dominant surface current path and determine the fundamental resonance in the lower Wi-Fi band. To improve the impedance bandwidth and radiation characteristics, a partial ground plane was used to support monopole behavior. Additionally, peripheral slots ware introduced along

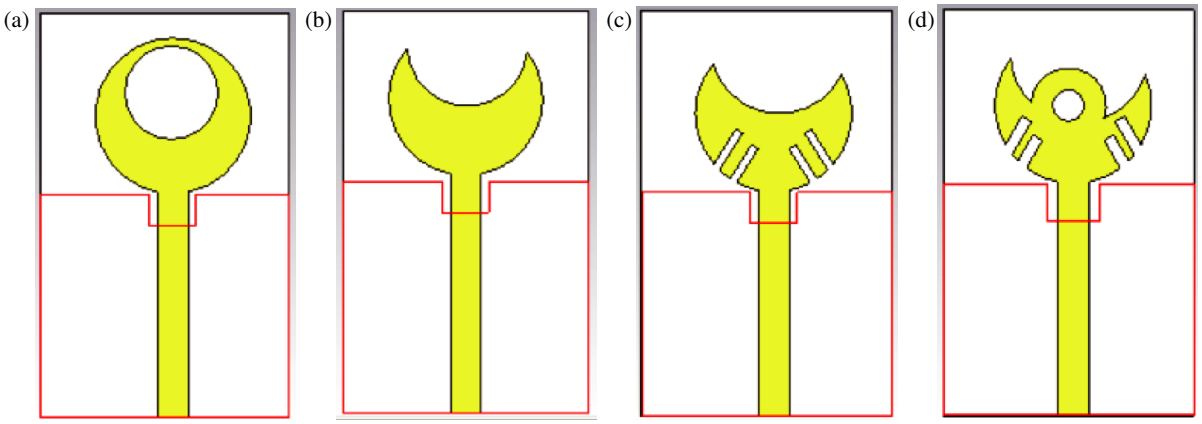

FIGURE 1. Evolution of the proposed antenna geometry: (a) Circular Patch with circular hole (CwCh); (b) Circular Crescent Patch (CC); (c) Circular Crescent Peripheral Slit Patch (CCPS); (d) Circular Crescent Peripheral Slit with Ring Patch (CCPSR).

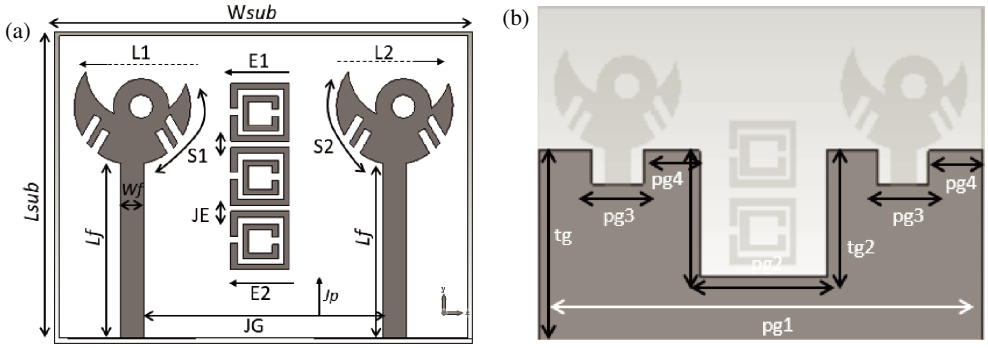

FIGURE 2. Proposed Wi-Fi patch antenna: (a) front view, (b) rear view.

the edges of the crescent radiator to effectively extend the surface current path. These modifications enabled the excitation of higher-order resonance modes, resulting in stable upper-band resonance at 5.8 GHz without increasing the physical size of the antenna.

All dimensional parameters summarized in Table 1 correspond to the optimized configuration used in the antenna design and simulation results presented in this study. The non-critical tuning variables and intermediate design values are omitted for clarity, whereas the listed parameters represent the essential physical dimensions required for fabrication and performance reproducibility. The use of a crescent-shaped geometry combined with edge slots allows the proposed antenna to achieve a compact size, stable dual-band operation, and better impedance performance than conventional microstrip antenna structures.

TABLE 1. Optimized geometric parameters of the proposed antenna.

Parameter	Value (mm)	Parameter	Value (mm)
L_{sub}	52	E_1	10.5
W_{sub}	70	E_2	10.5
L_f	30	J_E	2
W_f	4	pg_1	70
L_1	10	pg_2	20
L_2	10	pg_3	8
s_1	8.5	pg_4	5.2
s_2	8.5	tg	29.7
J_G	70	tg_2	19.7
J_p	2		

2.1. Antenna Design Evolution

To obtain dual-band characteristics, the antenna was designed through a gradual geometric evolution process consisting of four stages of structural modification as shown in Figure 1, while Figure 2 shows the antenna after being arranged in a 2×1 MIMO antenna by integrating a rectangular ring structure between the two elements and creating a rectangular hole structure on the ground plane. In the first stage (CwCh), concentric circular patches were used as the basic structure, producing one main resonance frequency. In the second stage (CC), part of the circle was cut to form a crescent geometry, which extended the surface current path and produced additional resonance modes.

In the third stage (CCPS), several slits were added to the edges of the crescent structure to improve the distribution and effective length of the current, resulting in improved impedance matching and bandwidth widening.

The final stage (CCPSR) added a circular element at the top as a coupling/matching structure to stabilize the input impedance and enhance dual-band performance. At each stage of evolution, the antenna performance was evaluated using

electromagnetic parameters, including the reflection coefficient (S_{11}), bandwidth, gain, and surface current distribution. The appearance of two different resonance frequencies on the S_{11} curve confirmed dual-band operation in the 2.4 and 5.8 GHz bands. Furthermore, surface current analysis shows that different parts of the structure dominate each resonance mode, explaining the formation of these two operating frequencies.

Figure 3 shows the reflection coefficient S_{11} for several antenna configurations in the 1–7 GHz frequency range. It shows that each structural modification results in different changes in the resonance response, both in terms of S_{11} depth and working bandwidth. The early models exhibited limited resonance and uneven impedance matching across the frequency band, whereas the final configuration exhibits clearer and more stable resonances that satisfied the -10 dB criterion at both Wi-Fi bands, confirming the effectiveness of the proposed geometry.

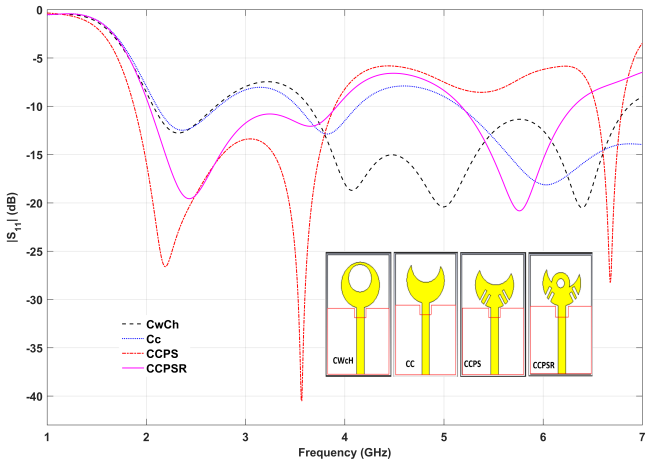

FIGURE 3. Simulated reflection coefficient S_{11} of the antenna element.

2.2. Peripheral Slit Configuration

The peripheral gap configuration on the proposed antenna was designed using a step-by-step approach to evaluate the effect of geometric modifications on the impedance characteristics and dual-resonance formation. This method allows for a clear understanding of the working mechanism of the peripheral gap in producing dual-band operation. In the initial stage (Step CwCh), the antenna was realized as a full-circle monopole patch supplied by a microstrip line. This structure served as a starting patch to determine the basic resonance frequency and initial response of the antenna. At this stage, the antenna produced only one dominant resonance with a relatively narrow bandwidth because the surface current path was still limited to the patch circle.

In Step CC, the center of the circular patch is removed to form a crescent-shaped patch. This modification expands the surface current path without increasing the physical size of the antenna. As a result, the resonance frequency shifts, and the impedance matching characteristics begin to improve, although the antenna still operates on a single main resonance band. In Step CCPS, two peripheral slots are added symmetrically on the left and right sides of the crescent patch, marked as S1 and S2. The addition of these slots acts as a disturbance to the surface current distribution, resulting in additional resonance modes. The interaction between the fundamental resonance in the crescent structure and the resonance induced by the peripheral slots begins to form multiresonance characteristics, although the frequency range separation is not yet fully optimal. The final stage (Step CCPSR) corresponds to the proposed antenna configuration, where the patch geometry is refined, including adjustment of the edge slot dimensions and formation of a center hole in the patch. The combination of the crescent structure, edge slots, and geometric modifications results in two separate and stable resonance bands, suitable for 2.4 GHz and 5.8 GHz Wi-Fi applications. In this configuration, the antenna shows a significant improvement in bandwidth and better impedance matching without a decrease in radiation pattern. The placement and dimensions of the edge slots are carefully designed to control the effective length of the surface current path and avoid a decrease in radiation performance. Longer slots increase the effective length of the current path, thereby lowering the resonance frequency, while variations in slot width affect the bandwidth and level of impedance matching. Therefore, the slot dimensions are optimized to achieve a balance between adequate bandwidth and radiation stability.

Overall, the addition of peripheral slots has proven effective in improving antenna performance by expanding the operational bandwidth and enabling the formation of a dual resonance without increasing the physical size of the antenna. This modification works by altering the surface current distribution and controlling the resonance mode, making the proposed antenna suitable for dual-band Wi-Fi applications with a compact and efficient structure.

3. RESULTS AND DISCUSSION

3.1. Ground Plane Evolution

To explain the working mechanism of the proposed antenna, a design evolution study was conducted by modifying the shape of the ground plane and the number of split-ring resonators (CSRRs) as shown in Figure 4. Two configurations are shown, a solid ground and a cut ground in the middle. In the first configuration, the ground was left intact so that the conductor areas at the bottom of the two antenna elements were connected. This condition allowed surface currents to spread freely from one element to another through the ground plane. Consequently, the central area continue ed acts as a shared propagation path, such that the electromagnetic interaction between the antenna elements remained strong.

In the second configuration, the center of the ground was cut to form a deep slit. This cut effectively separates the previously connected current paths, such that the current tends to be localized in the area of each element. In other words, the slit in the ground acts as both a physical and an electromagnetic barriers that limit current spreading in the central area of the structure. Additionally, the formation of the slit increases the effective current path length around the edges of the cut, which ultimately results in a more controlled field distribution in the region between the two elements.

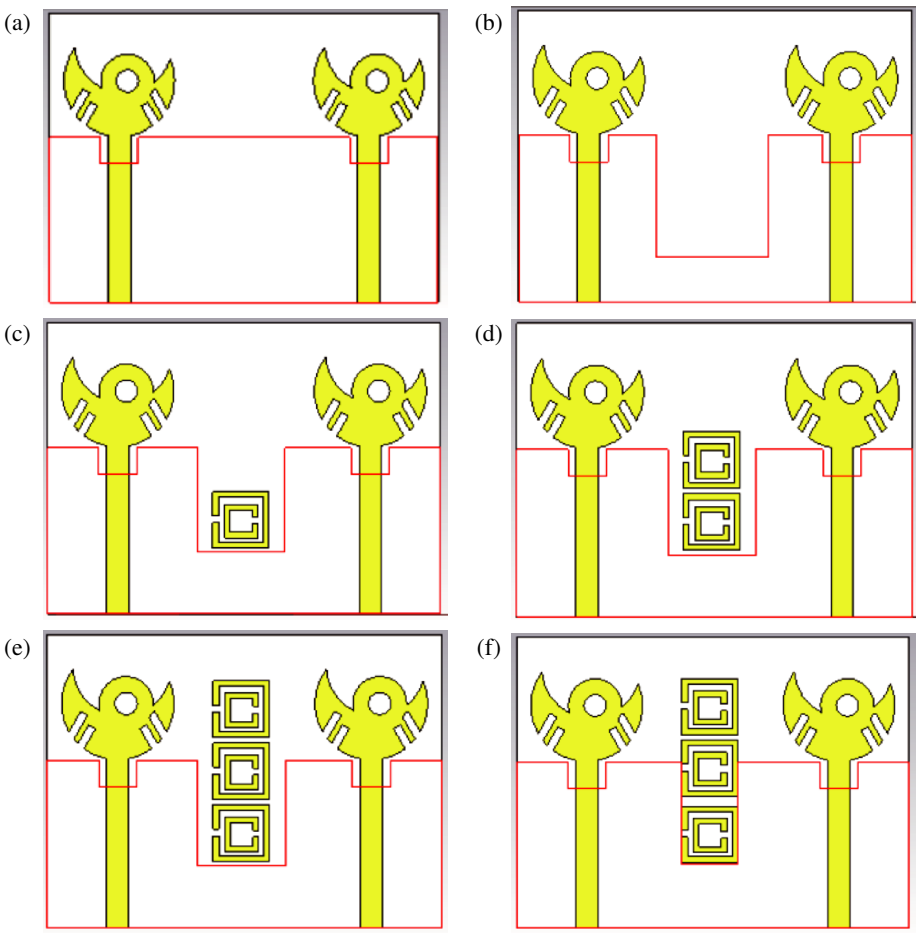

FIGURE 4. Design evolution with materials: (a) CCPSR1, (b) CCPSR2, (c) CCPSR3, (d) CCPSR4, (e) CCPSR5, (d) CCPSR6.

Overall, a comparison of the two configurations shows that ground engineering plays an important role in regulating the interaction between antenna elements. A continuous ground tends to allow for stronger coupling, whereas a cut ground helps separate current paths and stabilize MIMO system performance without the need to increase the antenna size. Therefore, the ground cutting technique can be considered a simple but effective design method for improving the performance of compact MIMO antennas.

3.2. Metamaterial Unit Cell

The application of metamaterials is a highly effective approach to improving antenna radiation performance, including the bandwidth, gain, and isolation between MIMO elements. The presence of metamaterials significantly affects surface waves, thereby causing the formation and control of additional resonant modes. The metamaterial unit cells proposed in this study are formed by adding concentrically arranged metal-coated bricks, rather than carving patterns into the substrate. The brick structure comprises square elements measuring $12 \times 12\,\text{mm}^2$ with a central opening of $10.5 \times 10.5\,\text{mm}^2$. Inside, $9 \times 9\,\text{mm}^2$ square bricks with a central opening of $8.5 \times 8.5\,\text{mm}^2$ are placed, along with a small gap of $1.2 \times 1.2\,\text{mm}^2$ in the center of the structure. These bricks are approximately 1 mm thick, such that the current paths and capacitive gaps form a distributed LC resonance network.

The metamaterial bricks were placed above the surface of the patch antenna at a distance of 1 mm, thereby allowing strong electric and magnetic field coupling between the patch antenna and the metamaterial structure. Identical cells can then be arranged in 1×2 and 1×3 vertical configurations to enhance the interaction with the antenna aperture without altering the ground plane.

When the antenna is excited, the surface current on the patch induces a dominant resonant mode in the layered brick structure. Around the resonance frequency, the effective impedance seen by the antenna changes, resulting in better impedance matching. This leads to a significant reduction in the reflection coefficient $|S_{11}|$ and an expansion of the -10-dB bandwidth in the 2.4 and 5.8 GHz bands compared with the reference antenna without metamaterial bricks. Additionally, the resonant nature of the structure reduces input-impedance fluctuations with frequency, resulting in more stable radiation characteristics across the operating band. The effective parameters of the metamaterial (μ_{eff}, ε_{eff}, and n_{eff}) are extracted from the complex S-parameters using standard retrieval techniques [17], showing strong dispersion around the resonance frequency and explaining the increased bandwidth and tuning characteristics obtained.

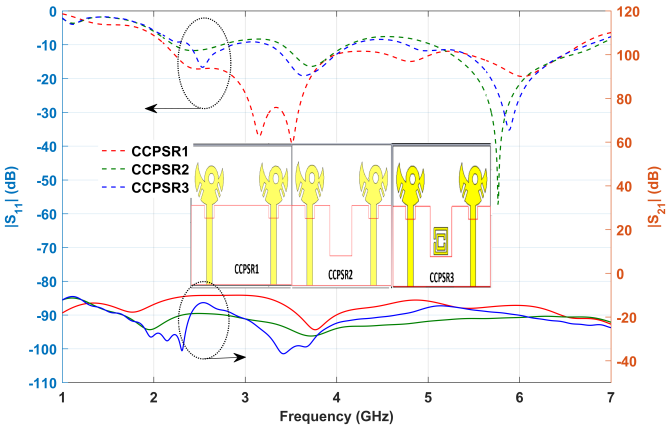

FIGURE 5. Simulated result of S_{11} and S_{21} of the CCPSR 1, 2 and 3.

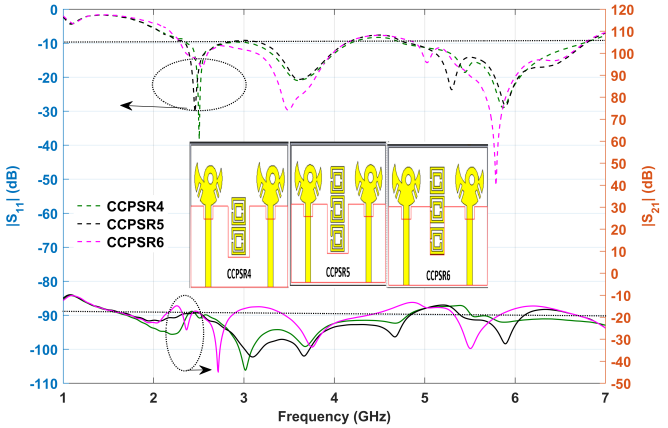

FIGURE 6. Simulated result of S_{11} and S_{21} of the CCPSR 4, 5 and 6.

3.3. Scatering Performance of Element and 2×1 MIMO Antenna

In the proposed MIMO scheme, two crescent-shaped transmitter elements are placed coplanar on an FR-4 substrate with a short inter-element distance to maintain a compact footprint. However, this proximity causes strong near-field interactions and surface current propagation on the ground plane, which in turn increases the mutual coupling, alters the impedance characteristics, and degrades the overall MIMO performance.

Adequate port isolation is required for realiable MIMO operation. Ideally, the transmission coefficient should satisfy

$$|S_{21}| \leq -20\,\text{dB}. \tag{1}$$

In the reference configuration (without additional structures), the isolation at 2.4 GHz remains between -7 and -12 dB. Therefore, a coupling-suppression mechanism is required without increasing the physical size of the antenna.

To mitigate this effect, a metamaterial-like resonant structure is inserted between the two transmitter elements. As reported in [21], the resonator can act as an artificial impedance path and can be modeled as

$$Z_{\text{meta}} = R_m + j\left(\omega L_m - \frac{1}{\omega C_m}\right), \tag{2}$$

where R_m, L_m, and C_m represent the equivalent resistance, inductance, and capacitance of the resonant structure, respectively.

This configuration effectively serves as a band-stop filter at the designed frequency. Consequently, the coupled surface current from one element is redirected back to the source, preventing its propagation to neighboring elements. This mechanism enhances isolation while maintaining compact dimensions and structural simplicity.

To analyze the mutual coupling between two CCPSR antenna elements, six design configurations are presented in Figure 4. The baseline model, shown in Fig. 4(a), consists of two elements separated by 70 mm with an intact ground plane, while Fig. 4(b) depicts the second model featuring a truncated ground. The subsequent designs, comprising the third through fifth models, integrate one, two, and three SRR units, respectively [Fig. 4(c)–(e)], to investigate their decoupling efficiency. This analysis concludes with the sixth model in Fig. 4(f), which utilizes a narrower ground slot than that of Fig. 4(e) to further optimize isolation performance. From Figure 5, it can be seen that CCPSR2 produces the best resonance frequency, namely $S_{11} = -57.22$ dB at a frequency of 5.76 GHz.

As shown in Figure 5, CCPSR1 produces S_{11} at a frequency of 2.4 GHz with a value of -16.97 dB and S_{21} of -10.42 dB. Although S_{11} at a frequency of 2.4 GHz is sufficient, the resulting S_{21} is still insufficient; therefore, a method is proposed with which the ground is cut in the middle as shown by CCPSR2. CCPSR2 produces S_{11} at a frequency of 2.4 GHz with a value of -11.71 dB, at a frequency of 3.6 GHz with a value of -17.65 dB, and at a frequency of 5.76 GHz with a value of -57.22 dB. PSRR2 produces the best S_{11} at a frequency of 5.76 GHz; however, at a frequency of 2.4 GHz, S_{11} is relative poor, although the resulting S_{11} is good at -18.52 dB. PSRR5 produces the best S_{11} of -30.36 dB at a frequency of 2.45 GHz and -27.51 dB at 5.87 GHz. PSRR5 also produces S_{21} with a value of -18.17 dB at a frequency of 2.4 GHz and -32.11 dB at a frequency of 5.8 GHz. Compared with PSRR1, it is observed that by providing three SRRs between two elements and making a wide ground cut, the mutual coupling performance can be increased by 7.75 dB at a frequency of 2.4 GHz and an increase in S_{21} of 17.08 dB at 5.8 GHz. Figure 6 illustrates the performance of CCPSRs 4–6. At 2.4 GHz, CCPSR 4 achieves an S_{11} of -30.37 dB and an S_{21} of -18.38 dB, whereas at 5.8 GHz, it exhibits an S_{11} of -28.5 dB and an S_{21} of -31.75 dB. Furthermore, the minimum S_{21} for CCPSR 4 is recorded as -38.1 dB at a frequency of 3.1 GHz. Among the various MIMO antenna configurations evaluated, CCPSR6 exhibits a superior S_{11} of -51.9 dB at 5.8 GHz; however, its performance at 2.4 GHz is less optimal at -14.18 dB. While CCPSR6 also achieves the best overall isolation (S_{21}) of -44.9 dB at 2.7 GHz, it does not align perfectly with our target dual-band requirements. Consequently, CCPSR4 is selected as the proposed design due to its more balanced and effective performance across both the 2.4 GHz and 5.8 GHz interest bands.

The surface current distribution further explains the isolation mechanism as shown in Figure 7. Without the resonator, the current spreads across the patch and ground plane and then cou-

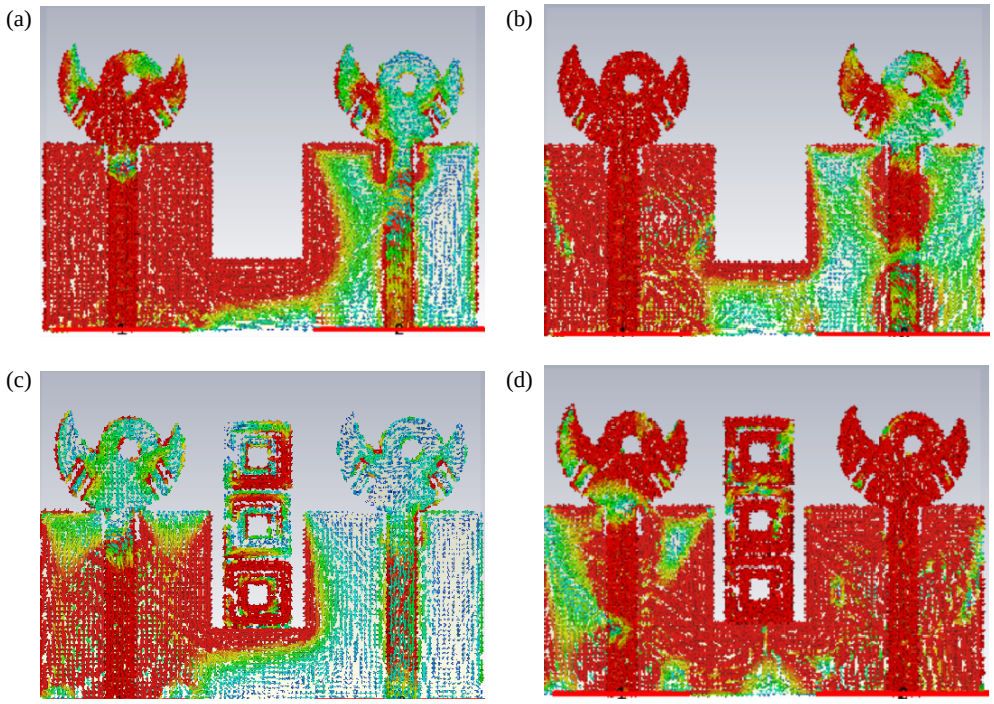

FIGURE 7. Surface current distribution of the proposed antenna: (a) CCPSR2 at 2.4 GHz, (b) CCPSR2 at 5.8 GHz, (c) CCPSR5 at 2.4 GHz and (d) CCPSR5 at 5.8 GHz.

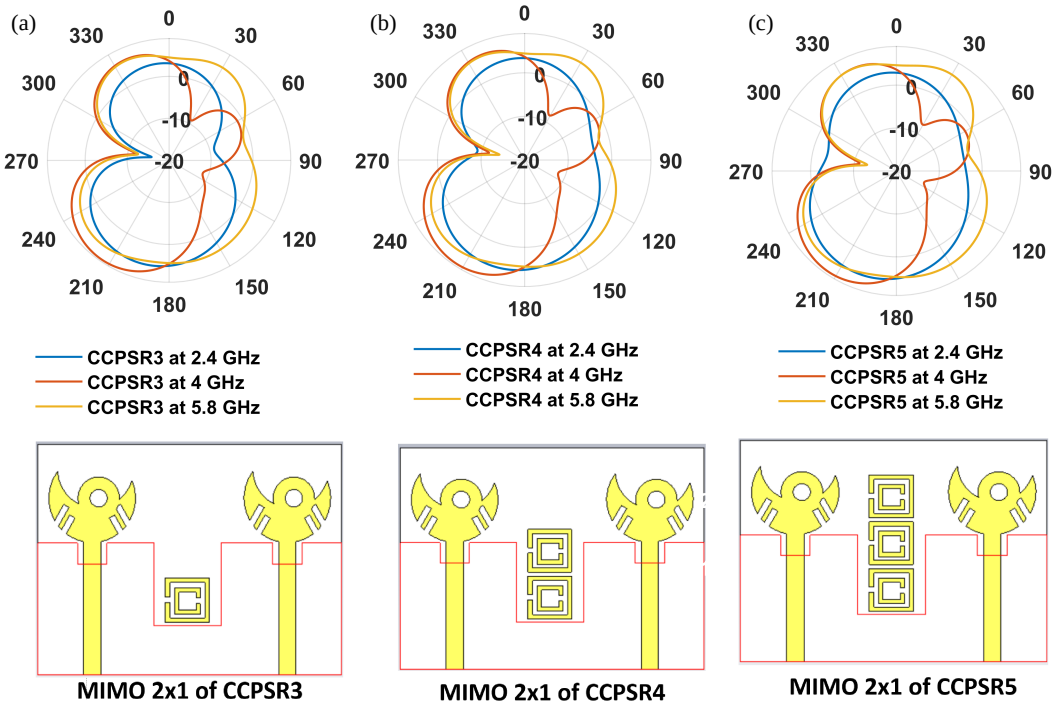

FIGURE 8. Simulated radiation pattern MIMO 2×1 at phi $= 90°$: (a) CCPSR3, (b) CCPSR4 and (c) CCPSR5.

ples to the neighboring elements. After inserting the metamaterial resonator, the current becomes concentrated in the central region; part of the energy is absorbed by the resonant structure, and the current path to the neighboring elements is effectively interrupted. At 2.4 GHz, the resonator extends the effective path length, contributing to band formation and improved matching. At 5.8 GHz, the structure behaves as a metasurface isolator, reflecting currents with opposite phase and thus enhancing isolation. Overall, the integration of metamaterial-like resonators provides three main advantages: (i) improved isolation without increasing antenna size, (ii) improved impedance stability, and (iii) preserved dual-band bandwidth. Therefore,

TABLE 2. Comparison of the proposed MIMO antenna with recent designs and their target applications.

Ref.	Size (mm^2)	Area (mm^2)	Frequency (GHz)	Gain Max (dB)	Number of Port (dB)	Isolation Max (dB)	Application
[22]	50×40	2000	2.12–2.8; 4.95–6.65	4.8	2	15–21	WLAN/WiMAX
[23]	40×24	960	5.725–5.875	–	2	24–34	WLAN 5.8 GHz
[24]	120×100	12000	2.45–2.82; 5.87–6.89	4	2	20	Pattern diversity
[25]	60×120	7200	6.4; 8.2	–	2	20	Plasmonic IC
[26]	52×194	10088	1; 0.7; 2.6; 3.1; 3.5	12.9	2	50	Low frequency automotive applications
[27]	99×50	4950	4	6.3	2	24.6	UWB systems
[28]	86×60	5160	5.9	8.3	2	29	V2X communications
[29]	140×70	9800	2–2.6; 3.4–3.6; 4.8–5	5–8	8	> 10	4G/5G/Sub-6 GH
[30]	130×130	152100	3.07–3.14	7.5	2	40	MIMO applications
[31]	100×55	5500	3.4–3.6	2.7	2	20–40	Mobile MIMO terminal
[32]	80×60	4800	0.9; 1.8; 2.3; 2.6	3–4	2	30	DCS, GSM and LTE
[33]	130×130	16900	1.08–4.05	2	2	31	MIMO systems
[34]	65×113	7345	2.41–2.49; 5.22–5.39	9.3	2	26.7 and 14	WLAN, MIMO antennas
[35]	95×105	9975	2.21–2.7	3.56	4	20	Wearable wireless, communication
Proposed work	**52×70**	3640	**2.4; 3.6; 5.3; 5.8; 6.4**	**8.3**	2	**38; 44.9**	**WLAN/IoT/Multi-standard wireless**

the proposed MIMO configuration is well-suited for modern dual-band Wi-Fi applications that require compact geometry and high isolation.

3.4. Radiation Pattern Characteristics

Radiation pattern analysis was performed to examine how the proposed antenna emits electromagnetic energy under different excitation conditions and to verify the effect of the metamaterial structure on beam formation. Measurements were performed in an anechoic chamber using a standard horn antenna as the receiving probe, where the antenna under test (AUT) was mounted on a rotary positioner. During the measurements, one port of the MIMO antenna was activated, whereas the other ports were terminated with a 50 Ω load to ensure realistic operating conditions in a multi-element environment. This procedure enables the evaluation of how inactive elements affect the total radiation and gain produced by the active elements.

Figure 8 illustrates the polar radiation patterns at $\phi = 90°$ for the 2×1 MIMO antenna configurations. The comparison includes CCPSR3, CCPSR4, and CCPSR5 types, which incorporate one, two, and three metamaterial units between the two antenna elements, respectively. From the simulation results, it is found that CCPSR3 produces mainlobe at frequencies of 2.4, 4, and 5.8 GHz of 5.39, 8.54, and 5.88 dBi, respectively; CCPSR4 mainlobe at frequencies of 2.4, 4, and 5.8 GHz of 5.39, 8.45, and 5.78 dBi, respectively; CCPSR5 mainlobe at frequencies of 2.4, 4, and 5.8 GHz of 5.51, 8.32, and 5.98 dBi, respectively. From the results obtained, it can be seen that CCPSR3 has the highest mainlobe, but CCPSR5 produces better resonance frequency performance than others at 2.4 GHz and 5.8 GHz frequencies. From the simulation results, it can be seen that the antenna has a very wide mainlobe direction, a large angular width, and a high side-lobe level, so a method is needed to optimize the radiation pattern as desired.

The simulation results show that the highest directivity of the antenna is 8.54 dBi at a frequency of 4 GHz. Directivity is a measure of an antenna's ability to focus energy in a certain direction compared to an isotropic antenna (which radiates in all directions). Directivity is purely geometric and does not take into account heat losses. Antenna radiation efficiency is a measure of how effectively an antenna converts input power into electromagnetic waves radiated into free space. This value is highly dependent on the antenna's operating frequency.

The radiation efficiency of an antenna takes into account losses due to material resistance (heat) and dielectric losses. Radiation efficiency is not constant and will increase with increasing frequency until it reaches the antenna's resonance point. However, efficiency can decrease again due to material (dielectric) losses. The CCPSR element has the highest radiation efficiency of 88% at a frequency of 2 GHz, while the MIMO 2 × 1 CCPSR has the highest radiation efficiency of 80% with a radiation efficiency at frequencies of 2.4 and 5.8 of 70%. So further research is needed to increase the radiation efficiency of the MIMO 2 × 1 CCPSR antenna.

The presence of the metamaterial structure slightly alters the current distribution and thus redistributes the radiated power, particularly in the higher frequency ranges. This effect contributes to better port isolation and stable radiation characteristics without causing unwanted pattern distortion. The measured patterns show that the proposed antenna is capable of maintaining pattern stability across the entire operating frequency range, with only minor deviations between the simulation and measurement curves. These deviations are mainly due to fabrication tolerances, connector losses, coaxial cable interference, and minor alignment errors during measurements in the test chamber.

Table 2 shows a comparison of several related references. Refs. [22, 23] have a smaller area than the antenna we purposed. However, Ref. [22] only works in dual frequency bands and has a maximum gain of 4.8 dB, while Ref. [23] only produces one frequency band at higher frequency than our antennas, with a minimum isolation of 34 dB. Ref. [24] to Ref. [35] have a larger area than the antenna we made. Antennas [27, 28, 30, 31, 33, 35] produce a single band while Ref. [25] produces dual bands. Ref. [26] produces 4 frequency bands and a higher gain than the antenna we made, but Ref. [26] has a very large antenna area. Ref. [27] has a larger size area than the antenna we purposed and only produces a single frequency band. It resonates at a frequency of 4 GHz with a narrow bandwidth, while our purposed antenna resonates at a lower frequency (start from 2.4 GHz) with a multiband frequency and a wide bandwidth. Ref. [32] has a relatively small size; however, it is still slightly larger than the proposed antenna. Additionally, it produces a lower maximum gain and fails to achieve the high isolation levels demonstrated in this work. The antennas we make have the advantage of small size, can work in multiband frequencies, and produce good maximum isolation performance. Overall, the proposed metamaterial-based MIMO antenna demonstrates the best balance among compact size, multi-band capability, high gain, strong isolation (up to 30 dB), and very low channel capacity loss. The use of metamaterial structures effectively suppresses surface current coupling between elements without increasing antenna dimensions. Therefore, the proposed design provides superior mutual coupling reduction and is more suitable for modern multi-standard WLAN wireless communication applications than the referenced work.

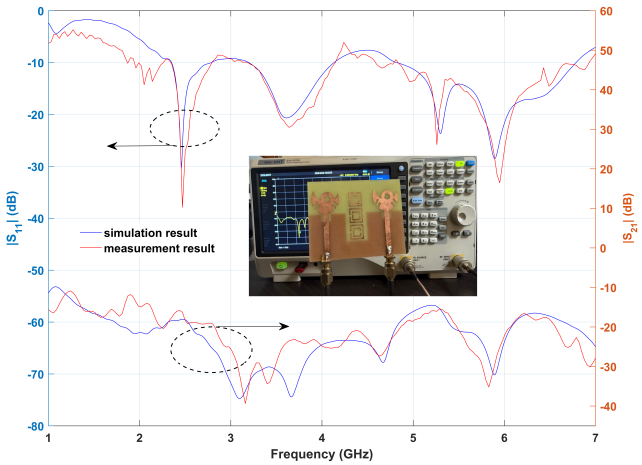

FIGURE 9. Simulated result of S_{11} and S_{21} of the CCPSR 4, 5 and 6.

4. EXPERIMENTAL PERFORMANCE EVALUATION

The measured $|S_{11}|$ and $|S_{21}|$ results are in good agreement with the simulation data, as illustrated in Figure 9, thereby validating the accuracy of the proposed design. The minor discrepancies observed between the simulated and measured results are primarily attributed to manufacturing tolerances, variations in the substrate's dielectric constant, and parasitic effects from the SMA connector soldering. To evaluate the antenna under real-world conditions, the prototype was integrated into a soil monitoring Internet of Things node comprising a microcontroller, pH sensor, soil moisture sensor, and wireless transmitter. The antenna served as the main transmitting element for transmitting sensor data to the receiver.

The device was placed directly on wet soil and vegetation to simulate an agricultural environment. This medium has high permeability and dielectric loss, which can cause antenna imbalance, impedance mismatch, and propagation attenuation. Therefore, this test represents a challenging and practical implementation scenario.

Calibration was performed using pH 4, 7, and 9 reference solutions with ten repeated measurements for each level. Table 3 summarizes the statistical results.

TABLE 3. pH calibration results.

Reference	Average	Absolute Error	Relative Error (%)
4	4.56	0.56	14.0
7	7.34	0.34	4.9
9	8.50	0.50	5.6

The maximum deviation was below 0.56 pH units, indicating acceptable accuracy for environmental monitoring applica-

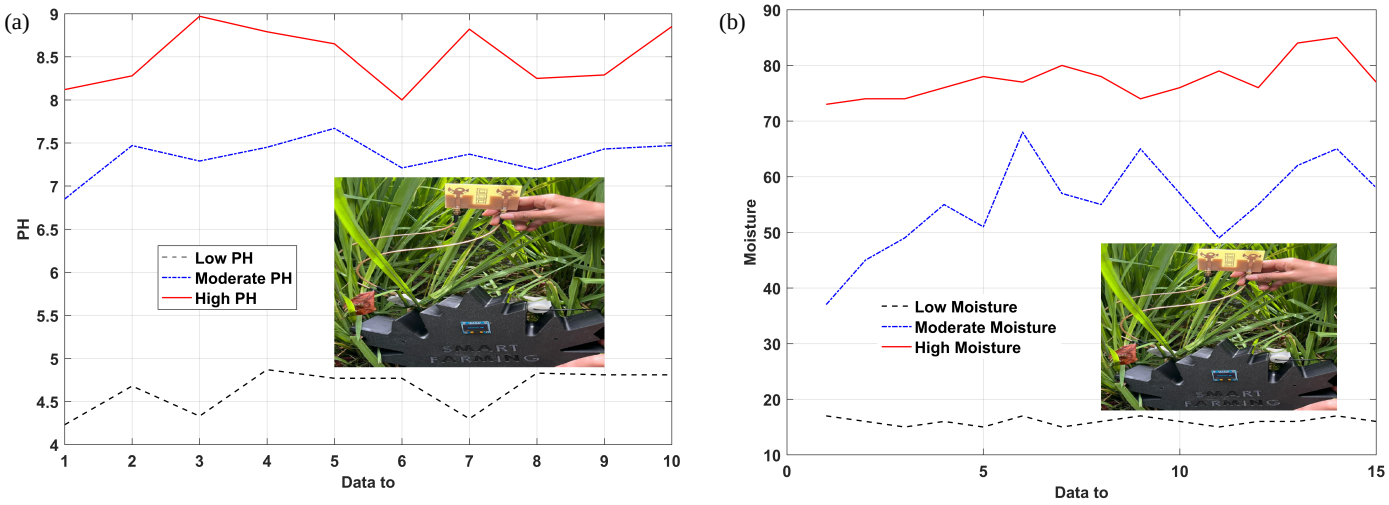

FIGURE 10. The hardware prototype integrates the proposed crescent-shaped antenna: (a) PH measurement result, (b) Moidture measurement result.

tions. Stable data transmission indicates that the antenna does not cause interference or data corruption.

Fifteen measurements were collected for dry, moist, and wet soil conditions as shown in Figure 10. The results are shown in Table 4.

TABLE 4. Soil moisture measurement statistics.

Condition	Range	Average %
Dry	15–18	16.0
Moist	37–68	55.2
Wet	73–85	77.4

Table 4 presents the data on soil moisture measurements classified into three main categories: Dry, Moist, and Wet. The values listed in this table are normalized sensor readings, making them dimensionless. Despite their masslessness, these values can be practically expressed as a percentage (%) to describe the level of water saturation relative to the maximum capacity the sensor can detect. This normalization simplifies the raw data onto a standard scale of 0–100% to facilitate interpretation of soil hydration status. In the Dry condition, the soil is at its lowest level, with a value ranging from 15% to 18% (average 16.0%), indicating very dry soil conditions. The Moist condition, which reflects the optimal water content for plants, has a value range of 37% to 68% with an average of 55.2%. Meanwhile, the Wet category showed the highest saturation level, with values ranging from 73% to 85% and an average of 77.4%. Expressing these values as a percentage allows users to more intuitively understand the proportion of water available in the soil for irrigation management purposes.

Overall, the antenna reliably operated even in degraded and highly conductive environments, demonstrating its suitability for smart agriculture applications. The close agreement between the measurement and the simulation results confirms proper impedance matching, high radiation efficiency, and accurate fabrication quality.

Communication range testing was conducted in an open field environment with line-of-sight (LOS) to determine the maximum transmission distance of the antenna system, as shown in Figure 11.

The transmitter node was placed at a reference location, and the receiver was gradually moved away. At each distance, the following parameters were recorded:

- Received Signal Strength Indicator (RSSI)
- Packet loss
- Latency
- Connection stability

Reliable communication was maintained up to approximately 250–260 m with a low packet loss. Low packet loss is a condition where the Packet Loss Ratio (PLR) is consistently below a critical threshold, typically set at less than 5%. Technically, this metric indicates that out of 100 transmitted data packets, at least 95 are successfully received by the receiver with intact data integrity. This percentage is considered a "low" standard because most communication protocols (such as acknowledgment mechanisms or packet retransmissions) can still handle such losses without burdening bandwidth or causing latency that disrupts overall system functionality. This communication robustness at a distance of 250–260 meters indicates that despite signal attenuation due to distance (path loss) and environmental interference, the Signal-to-Noise Ratio (SNR) remains above the device's sensitivity threshold. This minimal packet loss ensures that data streams remain synchronous and that connection failures do not occur, thus making the system operationally "reliable." By setting a quantitative value below 5%, the term "low" shifts from a merely qualitative claim to a technical standard that can be scientifically tested and verified.

The measured signal attenuation follows the free-space path loss model:

$$PL(\text{dB}) = 20\log_{10}(d) + 20\log_{10}(f) + 32.44 \qquad (3)$$

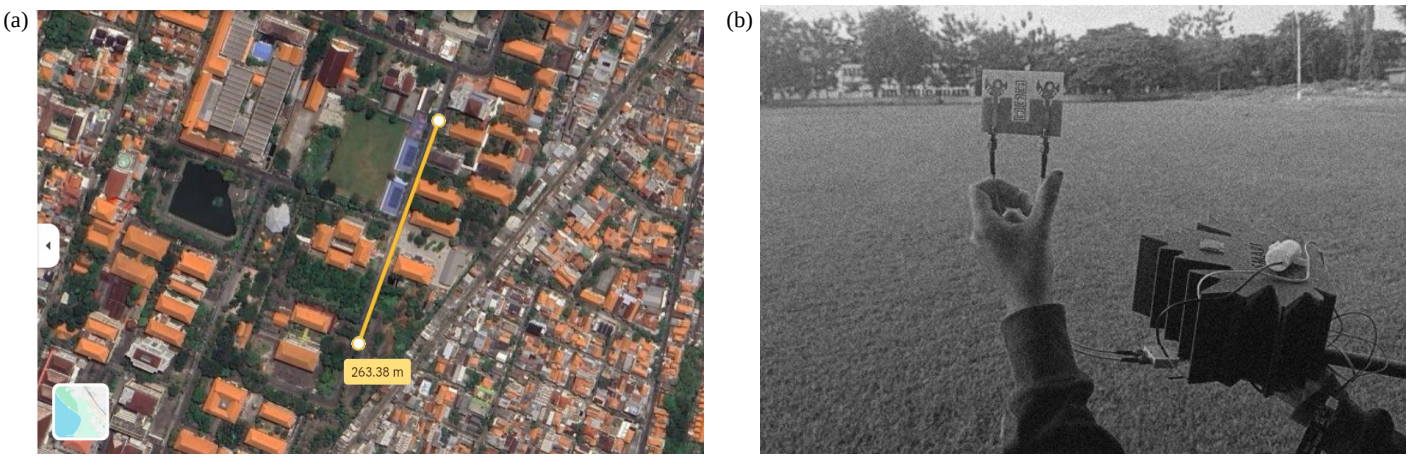

FIGURE 11. Evaluation of the communication range of the proposed antenna system. (a) Experimental line-of-sight (LOS) field test setup showing the placement of the transmitter and receiver, and (b) received signal strength indicator (RSSI) measured versus transmission distance. The results show stable communication performance up to approximately 250–260 m with gradual attenuation consistent with the free-space loss model.

where d is the distance (km), and f is the frequency (MHz).

The experimental results demonstrate that the antenna provides sufficient gain and radiation efficiency for medium-range outdoor Internet of Things IoT monitoring.

Combined calibration, laboratory characterization, and field testing show that the proposed antenna satisfies electromagnetic design requirements and practical implementation needs. Accurate sensor readings, stable wireless transmission, and reliable communication range collectively demonstrate the antenna's robustness for real-time environmental monitoring and smart farming systems.

5. CONCLUSION

A compact dual-band crescent-shaped microstrip antenna operating at 2.4/5.8 GHz was successfully designed, analyzed, and extended to a MIMO configuration using enhancement techniques inspired by metamaterials. The proposed antenna integrates a crescent-shaped radiator, peripheral edge slots, and a central resonant structure on a low-cost FR-4 substrate, enabling stable dual-band operation with improved impedance matching and compact dimensions. The final design exhibited reflection coefficients below -10 dB across frequency 2.35–2.78, 3.2–4.14, and 4.82–6.81 GHz, with minimum S_{11} values reaching approximately -30 dB at 2.4 GHZ, -20.7 dB at 3.6 GHz, -23.65 dB (at 5.29 GHz), and -16.38 dB at 6.4 GHz. This frequency can be used for Industrial, Scientific, and Medical (ISM) band, C-band/mid-band 5G, Wi-Fi 5 GHz lower/upper, and Wi-fi 6E/Wi-Fi 7. The radiation characteristics remain quasi-omnidirectional at 2.4 GHz and became more directive at 5.8 GHz, which is beneficial for wide indoor coverage and high-speed data links. The use of metamaterial-like resonant cells effectively changed the surface current distribution and input impedance, resulting in a wider bandwidth and smoother S-parameter response. In MIMO configurations, the embedded resonator significantly improved port isolation, increasing $|S_{21}|$ from approximately 7.75 dB and 17.08 dB at 2.4 and 5.8 GHz in the reference design to a value greater than -25 dB, while maintaining dual-band performance and compact size. Overall, the proposed antenna demonstrates a favorable balance among size, bandwidth, radiation performance, and isolation compared to recently reported designs, making it a robust and practical candidate for modern dual-band Wi-Fi applications.

ACKNOWLEDGEMENT

This research is funded by the Indonesian Endowment Fund for Education (LPDP) on behalf of the Indonesian Ministry of Higher Education, Science, and Technology, and is administered under the EQUITY Program (Contract No. 4312/B3/DT.03.08/2025).

REFERENCES

[1] Lopez-Perez, D., A. Garcia-Rodriguez, L. Galati-Giordano, M. Kasslin, and K. Doppler, "IEEE 802.11 be extremely high throughput: The next generation of Wi-Fi technology beyond 802.11 ax," *IEEE Communications Magazine*, Vol. 57, No. 9, 113–119, 2019.

[2] Telecom Advisory Services, LLC, "Global economic value of Wi-Fi," Tech. Rep., Available: https://www.globenewswire.com/news-release/2018/10/09/1618443/0/en/Wi-Fi-global-economic-value-reaches-1-96-trillion-in-2018.html, 2018.

[3] Federal Communications Commission, "FCC opens 6 GHz band to Wi-Fi and other unlicensed uses," Available: https://www.fcc.gov/document/fcc-opens-6-ghz-band-wi-fi-and-other-unlicensed-uses, 2020.

[4] European Commission, Directorate-General for Communications Networks, "Mandate to cept for harmonised conditions in the 5925–6425 MHz band," Available: http://ec.europa.eu/newsroom/dae/document.cfm?doc_id=50343, 2017.

[5] Au, E., "Specification framework for tgbe," https://mentor.ieee.org/802.11/dcn/19/11-19-1262-23-00be-specification-framework-for-tgbe.docx, Jan. 2021.

[6] Nurhayati, N., T. Rijanto, P. W. Rusimamto, A. Abimanyu, S. P. J. Christydass, and A. Paleologoudias, "Impedance band-

width enhancement of monopole antenna with triangle slot in the ground plane and modified patch for UWB applications," in *2021 3rd International Conference on Research and Academic Community Services (ICRACOS)*, 301–304, Surabaya, Indonesia, 2021.

[7] Roy, A., S. Bhunia, D. C. Sarkar, and P. P. Sarkar, "Slot loaded compact microstrip patch antenna for dual band operation," *Progress In Electromagnetics Research C*, Vol. 73, 145–156, 2017.

[8] Hoang, T. V., T. T. Le, Q. Y. Li, and H. C. Park, "Quad-band circularly polarized antenna for 2.4/5.3/5.8-GHz WLAN and 3.5-GHz WiMAX applications," *IEEE Antennas and Wireless Propagation Letters*, Vol. 15, 1032–1035, 2015.

[9] Fernandes, E. M. F., M. W. B. da Silva, L. da Silva Briggs, A. L. P. de Siqueira Campos, H. X. de Araújo, I. R. S. Casella, C. E. Capovilla, V. P. R. M. Souza, and L. J. de Matos, "2.4–5.8 GHz dual-band patch antenna with FSS reflector for radiation parameters enhancement," *AEU — International Journal of Electronics and Communications*, Vol. 108, 235–241, 2019.

[10] Nurhayati, G. Hendrantoro, T. Fukusako, and E. Setijadi, "Mutual coupling reduction for a UWB coplanar vivaldi array by a truncated and corrugated slot," *IEEE Antennas and Wireless Propagation Letters*, Vol. 17, No. 12, 2284–2288, 2018.

[11] Zhou, Y. and Y. Zheng, "A high-gain and dual-band compact metasurface antenna for Wi-Fi/WLAN applications," *Materials*, Vol. 18, No. 11, 2538, 2025.

[12] Olan-Nuñez, K. N. and R. S. Murphy-Arteaga, "Dual-band antenna on 3D-printed substrate for 2.4/5.8 GHz ISM-band applications," *Electronics*, Vol. 12, No. 11, 2368, 2023.

[13] Jin, L. and R. Zhang, "A dual-band wideband high-gain slot loaded microstrip patch antenna," *AEU — International Journal of Electronics and Communications*, Vol. 177, 155193, 2024.

[14] Nurhayati, N., F. Y. Zulkifli, E. Setijadi, B. E. Sukoco, M. N. M. Yasin, and A. M. D. Oliveira, "Bandwidth, gain improvement, and notched-band frequency of SWB Wave Coplanar Vivaldi antenna using CSRR," *IEEE Access*, Vol. 12, 16 926–16 938, 2024.

[15] Nurhayati, N., A. M. d. Oliveira, W. Chaihongsa, B. E. Sukoco, and A. K. Saleh, "A comparative study of some novel wideband tulip flower monopole antennas with modified patch and ground plane," *Progress In Electromagnetics Research C*, Vol. 112, 239–250, 2021.

[16] Zulkifli, F. Y. and M. W. Iqbal, "Bandwidth and gain enhancement of microstrip leaky-wave antennas with slot and defected ground structure," *Journal of Engineering & Technological Sciences*, Vol. 55, No. 3, 289–299, 2023.

[17] Kumar, S. and H. Singh, "A comprehensive review of metamaterials/metasurface-based MIMO antenna array for 5G millimeter-wave applications," *Journal of Superconductivity and Novel Magnetism*, Vol. 35, No. 11, 3025–3049, 2022.

[18] Kumar, A., A. Q. Ansari, B. K. Kanaujia, J. Kishor, and L. Matekovits, "A review on different techniques of mutual coupling reduction between elements of any MIMO antenna. Part 1: DGSs and parasitic structures," *Radio Science*, Vol. 56, No. 3, 1–25, 2021.

[19] Alam, M. M., R. Azim, N. M. Sobahi, A. I. Khan, and M. T. Islam, "A dual-band CPW-fed miniature planar antenna for S-, C-, WiMAX, WLAN, UWB, and X-band applications," *Scientific Reports*, Vol. 12, No. 1, 7584, 2022.

[20] Mahdjoubi, K., E. Penard, J. P. Daniel, and C. Terret, "Mutual coupling between circular disc microstrip antennas," *Electronics Letters*, Vol. 23, No. 1, 27–28, 1987.

[21] Khan, D., A. Ahmad, and D.-Y. Choi, "Dual-band 5G MIMO antenna with enhanced coupling reduction using metamaterials," *Scientific Reports*, Vol. 14, No. 1, 96, 2024.

[22] Peng, H., R. Zhi, Q. Yang, J. Cai, Y. Wan, and G. Liu, "Design of a MIMO antenna with high gain and enhanced isolation for WLAN applications," *Electronics*, Vol. 10, No. 14, 1659, 2021.

[23] Nirmal, P. C., A. Nandgaonkar, and S. Nalbalwar, "Mutual coupling reduction between H shaped compact MIMO antenna for WLAN application," *International Journal of Wireless and Microwave Technologies*, Vol. 7, No. 6, 46–57, 2017.

[24] Liu, X., Y. Wu, Z. Zhuang, W. Wang, and Y. Liu, "A dual-band patch antenna for pattern diversity application," *IEEE Access*, Vol. 6, 51 986–51 993, 2018.

[25] Pan, B. C. and T. J. Cui, "Broadband decoupling network for dual-band microstrip patch antennas," *IEEE Transactions on Antennas and Propagation*, Vol. 65, No. 10, 5595–5598, 2017.

[26] Kumar, A., G. Singh, M. K. Abdulhameed, S. R. Hashim, and A. J. A. Al-Gburi, "Development of fractal 5G MIMO antenna for sub 6 GHz wireless automotive applications," *Progress In Electromagnetics Research M*, Vol. 130, 121–128, 2024.

[27] Das, P., C. Saha, and K. Mandal, "Mutual coupling and RCS reduction of MIMO antenna using a hybrid technique," in *2022 IEEE Wireless Antenna and Microwave Symposium (WAMS)*, 1–5, Rourkela, India, 2022.

[28] Aliqab, K., A. Armghan, M. Alsharari, and M. H. Aly, "Highly decoupled and high gain conformal two-port MIMO antenna for V2X communications," *Alexandria Engineering Journal*, Vol. 74, 599–610, 2023.

[29] Hou, J., Y. Peng, J. Huang, Z. Wang, and T. A. Denidni, "MIMO 5G smartphone antenna with tri-band and decoupled elements," *Sensors*, Vol. 23, No. 11, 5186, 2023.

[30] Dai, X. W., W. H. Hu, H. Hong, and G. Q. Luo, "High isolation MIMO antenna designed with tightly coupled microstrip patch pairs," *AEU – International Journal of Electronics and Communications*, Vol. 177, 155169, 2024.

[31] Zhao, X., S. P. Yeo, and L. C. Ong, "Decoupling of inverted-F antennas with high-order modes of ground plane for 5G mobile MIMO platform," *IEEE Transactions on Antennas and Propagation*, Vol. 66, No. 9, 4485–4495, 2018.

[32] Yang, Y., Q. Chu, and C. Mao, "Multiband MIMO antenna for GSM, DCS, and LTE indoor applications," *IEEE Antennas and Wireless Propagation Letters*, Vol. 15, 1573–1576, 2016.

[33] Zhu, S., Y. Shao, Z. Li, X. Wang, X. Bi, Y. Song, and Z. Quan, "Synergistically optimized Vivaldi array with SSPP decoupling and metasurface gain enhancement," *Progress In Electromagnetics Research Letters*, Vol. 129, 35–41, 2026.

[34] Xu, J. and Y. Wang, "A defected ground structure design for reducing coupling in dual-band MIMO antennas," *Progress In Electromagnetics Research C*, Vol. 158, 93–101, 2025.

[35] Yu, Y., Y. Dong, Y. He, and Y.-F. Cheng, "A high-isolation optically transparent 2 × 2 antenna array using metal mesh material," *Micromachines*, Vol. 16, No. 5, 528, 2025.